

Consistency Diffusion Models for Single-Image 3D Reconstruction with Priors

Chenru Jiang^{*,1,3}, Chengrui Zhang^{*,1,2}, Xi Yang¹, Jie Sun¹, Yifei Zhang⁴, Bin Dong³, Kaizhu Huang^{†3}
¹Xi'an Jiaotong-Liverpool University, ²University of Liverpool, ³Duke Kunshan University, ⁴Ricoh Software

Chenru.Jiang, Kaizhu.Huang, Bin.Dong@dukekunshan.edu.cn yifei.zhang@cn.ricoh.com

Chengrui.Zhang18@student.xjtlu.edu.cn, Jie.Sun, Xi.Yang01@xjtlu.edu.cn

Abstract

This paper delves into the study of 3D point cloud reconstruction from a single image. Our objective is to develop the Consistency Diffusion Model, exploring synergistic 2D and 3D priors in the Bayesian framework to ensure superior consistency in the reconstruction process, a challenging yet critical requirement in this field. Specifically, we introduce a pioneering training framework under diffusion models that brings two key innovations. First, we convert 3D structural priors derived from the initial 3D point cloud as a bound term to increase evidence in the variational Bayesian framework, leveraging these robust intrinsic priors to tightly govern the diffusion training process and bolster consistency in reconstruction. Second, we extract and incorporate 2D priors from the single input image, projecting them onto the 3D point cloud to enrich the guidance for diffusion training. Our framework not only sidesteps potential model learning shifts that may arise from directly imposing additional constraints during training but also precisely transposes the 2D priors into the 3D domain. Extensive experimental evaluations reveal that our approach sets new benchmarks in both synthetic and real-world datasets. The code is included with the submission.

1. Introduction

3D object reconstruction has been a long-standing challenge in computer vision, yet serving as a critical component in many real-world applications, such as robotic control [9], human-computer interaction [28, 43], and 3D object editing [4]. Once multiple views of 2D images are available, current reconstruction methods have shown superior performance. However, when only a single-view 2D image is available, the limited priors often lead to significant structural ambiguity and detail deficiencies in the reconstructed output, making it challenging to maintain struc-

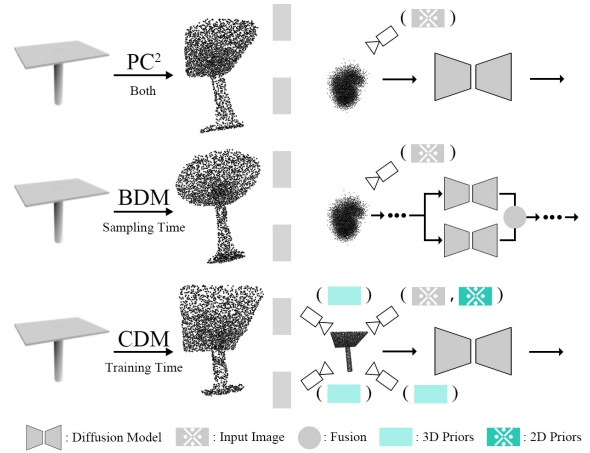


Figure 1. Illustration of reconstruction results comparison and network structures. Left: the reconstruction results of PC², BDM, and our CDM. Right: the network structures of the three approaches. BDM focuses on randomly merging the outputs of two models during the sampling phase, while our method leverages tailored 2D and 3D priors to promote structural consistency on the reconstruction process during training.

tural consistency with the target object.

In recent years, a significant amount of research has focused on using traditional convolutional models for 3D reconstruction tasks from one single image [18, 24, 34, 46, 50]. These methods typically reconstruct 3D objects in a voxelized form based on information from an image. However, such approaches often result in small-scale, low-resolution voxel representations, limiting the quality and details of the reconstructed objects. Recently, some works [16, 18, 39, 50] have also utilized implicit representations and radiance fields. These methods are capable of rendering novel views with photorealistic quality but still often fail to reconstruct the possible 3D shape distribution from just one single input image. The rise of diffusion models in 2D computer vision has sparked interest in their application to 3D object generation from a single image input. Moreover, diffusion models excel at capturing complex

*Equal Contribution

†Corresponding author

geometric shapes by explicitly modeling the data distribution’s probability density. This capability allows diffusion models to iteratively refine 3D structures through a denoising process, making them particularly adept at handling the challenges of single-view image input. Traditional models, in contrast, often produce incomplete or blurry structures due to their single-step generation process.

PC² [33] is the first to directly apply the conditional diffusion model to tackle 3D point cloud reconstruction. As shown in the right top part of Fig. 1, the feature of single image is used as the condition, which is projected on the point cloud, to train the diffusion model for predicting the Gaussian noise. We observed that, on average, only 55% of the points have initial features before training, while the initial features of the remaining points are set to zero. Thus, using only one image as a condition often results in insufficient 2D priors and weak constraints on reconstruction consistency, thereby limiting the model’s performance. A subsequent variant, BDM [49], focuses on incorporating the outputs of a pre-trained model as extra priors with the outputs of PC² model in sampling time for obtaining the final reconstruction results. The model structure of BDM is shown in the right middle part of Fig. 1. However, the results from the pre-trained network are class-level reconstruction, and BDM adopts a random combination strategy to merge the outputs of the two models. Consequently, this non-specific incorporation of priors still provides weak constraints on reconstruction consistency. Currently, diffusion-based reconstruction models struggle to effectively control output diversity, further hindering their ability to maintain consistent reconstruction quality.

In this work, we propose a novel Bayesian diffusion model, termed as Consistency Diffusion Model (CDM), which utilizes both 2D and 3D priors within a Bayesian framework to enhance the consistency constraint. As shown in the bottom-right of Fig. 1, multi-viewpoint structural priors derived from the initial point cloud are utilized as additional object-level 3D priors. One of the key contributions of this work is a new bound term in the function derivation. This term leverages the 3D priors to continually narrow the distribution gap between the point cloud posteriors $p_\theta(x_t)$ and priors $p_\theta(x_0)$, thereby increasing the evidence lower bound (ELBO) of reconstruction probability and strengthening consistency learning during diffusion training. Specifically, the distance between the 3D priors and 3D posteriors is calculated and used as the loss value during the model’s gradient descent process. This method effectively ensures that reconstruction consistency is maintained during the reverse process at any timestep, while adding only a negligible amount of computational overhead.

In terms of 2D priors, we further explore leveraging information from a single image in order to provide more effective initial data during the training phase. Our empir-

ical findings indicate that different 2D priors yield varying performance outcomes depending on the feature distributions of the datasets. For real-world data, we use the DINO v2 [37] to accurately extract depth information from the single image, and the additional 2D prior features notably improve reconstruction quality. However, on synthetic datasets, a distribution shift between the data and DINO v2’s training data caused the extracted depth information to be less effective. In such cases, we instead focus on extracting precise contour information. These additional features are then combined with image features and projected to the point cloud, providing precise guidance for the training of the diffusion model.

Furthermore, we design a variety of experiments to evaluate the advantages and limitations of different approaches and strategies for this task. For instance, we investigate critical issues such as the effectiveness of embedding information from images or text, the impact of textures and depth priors on reconstruction quality, and how 2D priors can be more effectively utilized in 3D space. Extensive experiments demonstrate that our method achieves state-of-the-art (SOTA) performance on both synthetic and real-world data.

It is worth noting that the proposed CDM relies solely on extracting 2D and 3D priors from the training data, without utilizing any auxiliary information. Additionally, empirical results demonstrate that the performance of CDM can be significantly enhanced with pre-trained model like BDM. The main contributions of this work are three-fold: 1) Integration of 3D Priors via maximizing ELBO; 2) Exploitation of more precise 2D priors; 3) Empirical validation and superior performance.

2. Related Work

2.1. 3D Shape Reconstruction

In early research, 3D shapes were reconstructed by extracting multi-modal information, such as shading [1, 17], texture [47], and silhouettes [6]. On one hand, some works [12, 13, 21, 23, 44] perform 3D reconstruction task using either regression [23] or retrieval [44] approaches. Other works initially leverage image geometry techniques for multi-view reconstruction [15], then decode the extracted features using 3D CNN to generate 3D data representations such as voxel grids [7, 20, 48].

Recently, a new research direction focusing on differentiable rendering has gained increasing popularity (e.g., NeRF [35]). Most studies in this area rely on abundant multi-view data to reconstruct target scenes. However, some recent works [3, 16, 18, 19, 22, 29, 39, 50] have shifted focus toward learning cross-scene priors to handle the reconstruction of sparse-view scenes. Among them, works closely related to our study, such as NeRF-WCE [16] and PixelNeRF [50], have attempted NeRF scene recon-

struction from limited or single-view inputs. While these methods perform well under the few-view condition, single-view reconstruction remains a highly challenging and ill-posed problem, making it difficult for these approaches to achieve strong performance in such settings.

In our work, we adopt an entirely different approach from the aforementioned methods. We extract more initial priors to guide the training of diffusion models, enabling direct 3D point cloud reconstruction. Owing to the probabilistic nature of diffusion models, they can effectively capture the ambiguity of unseen regions while also generating high-resolution 3D point cloud shapes.

2.2. Diffusion Model for 3D Reconstruction

Image-to-3D reconstruction aims to create 3D assets from images, essentially making it a 3D generation task with 2D conditions. Recently, many works have introduced an intermediate stage that generates multi-view images before reconstructing the 3D shape. For instance, One-2-3-45 [26] leverages the 2D diffusion model Zero-1-to-3 [27] to generate 4 posed images and trains a neural network to represent the 3D shape. One-2-345++ [25] fine-tunes Stable-Diffusion to generate 6 posed tile images at once, improving the cross-view consistency. SyncDreamer [30] synchronizes the intermediate states of generated multi-view images at each step of the reverse diffusion process, using a 3D-aware feature attention mechanism that correlates features across different views.

However, these methods generally require high computational resources, and their reconstruction performance heavily depends on the quality of the generated multi-view images. This makes it challenging to precisely and effectively control the volume of the reconstructed objects. In contrast, our work eliminates the need for this intermediate multi-view generation stage, directly generating the point cloud from a single 2D image.

2.3. Diffusion Model for 3D Point Cloud

Currently, 3D point cloud reconstruction remains an area in need of further exploration, with only a limited number of studies conducted. In the field of unconditional point cloud generation, recent research has not addressed the issue of performing 3D reconstruction based on images from real-world scenes [31, 32, 45, 53].

In conditional point cloud generation, a pioneering work is PC² [33], which projects encoded 2D features onto 3D point clouds as control conditions to guide the training of 3D point cloud diffusion models. The results of this work demonstrate the effectiveness of point cloud diffusion models on both real and synthetic datasets. Subsequent works have followed the structure of PC². For example, CCD-3DR [10] improves local feature alignment using a centered diffusion probabilistic model, while BDM [49], based on

Bayesian statistical theory, employs an unconditional pre-trained diffusion model alongside the PC² diffusion model and then performs random selection to blend the outputs from both models. However, in the task of conditional 3D point cloud reconstruction, current works neither investigate 3D priors nor explore additional 2D priors, leading to weak constraints on reconstruction consistency.

Yet, rich and effective priors can often significantly enhance model performance. Therefore, we attempt to introduce rich priors from 2D diffusion models, focusing on methods for deeply exploring initial information. Our proposed framework not only integrates effective 2D priors but also excavates 3D priors from the initial point cloud, enabling effective constraints on reconstruction consistency during diffusion training.

3. Method

This section will provide a detailed explanation of our method, with Fig. 2 visually illustrating our network structure. Initially, we will briefly review the denoising diffusion model applied to point cloud data and discuss the key observations and motivations driving our approach. Subsequently, we will focus on the extraction of 3D priors from the initial point cloud and describe how we construct a bound term to align the data distributions between the posteriors and priors of the point cloud at any timestep t , thereby constraining the diffusion model to learn reconstruction consistency. Concluding this section, we will delve into how to further extract additional 2D priors from the image and effectively integrate them into the diffusion model for guiding the training process.

3.1. Preliminaries of Point Cloud Diffusion Models

Diffusion models serve as general-purpose generative frameworks that progressively introduce noise to a sample from a target distribution, $x_0 \sim q(x_0)$, following a series of steps determined by a variance schedule. The noise addition at each step follows a Gaussian distribution. The details of the forward and reverse process can be expressed as:

$$\begin{aligned}
 q(x_{1:T}|x_0) &:= \prod_{t=1}^T q(x_t|x_{t-1}), \\
 p_\theta(x_{0:T}) &:= p(x_T) \prod_{t=1}^T p_\theta(x_{t-1}|x_t).
 \end{aligned}
 \tag{1}$$

In the context of the 3D field, a point cloud with N points is treated as a $3N$ dimensional object. A diffusion model $p_\theta : \mathbb{R}^{3N} \rightarrow \mathbb{R}^{3N}$ is trained to denoise the point positions, starting from an initial Gaussian noise distribution. At each step, the network predicts the offset from the current position of each point, iteratively refining the point cloud to approximate a sample from $q(x_0)$. The network

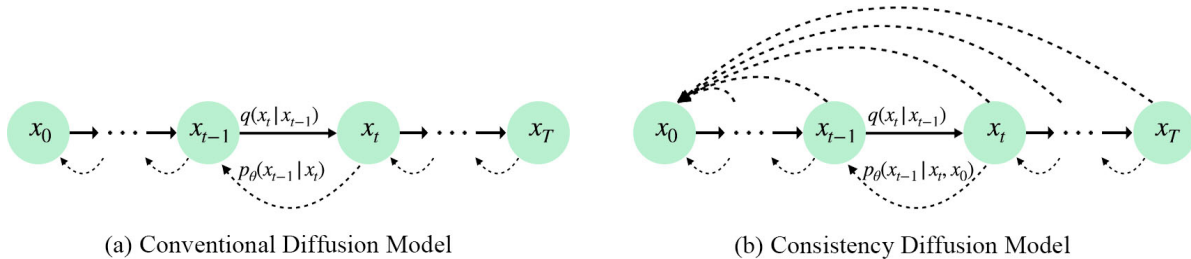


Figure 2. Model structure of conventional diffusion model and our consistency diffusion model.

is trained by minimizing the L_2 loss between the predicted noise $\epsilon \in \mathbb{R}^{3N}$ and the true noise added in the time step t :

$$\mathcal{L} = \mathbb{E}_{\epsilon \sim \mathcal{N}(0, \mathbf{I})} [\|\epsilon - p_\theta(x_t, t)\|_2^2]. \quad (2)$$

PC² [33] attempts to reconstruct 3D point clouds by using a single 2D image as a condition within a point cloud diffusion model. This approach employs the camera parameters of the 2D image to rotate the noisy point cloud (x_t) so that it aligns with the viewpoint from which the image is captured. Subsequently, a pixel-to-point projection operation is performed on the image features, which serves as a condition to guide the diffusion training. This conditional distribution can be expressed as $q(x_0|I, V)$. The model structure of PC² is similar with subfigure (a) in Fig. 2 and the loss function can be expressed as:

$$\mathcal{L}_{\text{PC}^2} = \mathbb{E}_{\epsilon \sim \mathcal{N}(0, \mathbf{I})} [\|\epsilon - p_\theta(x_t, t, I, V)\|_2^2]. \quad (3)$$

Unfortunately, due to the limitation of a single viewpoint, a significant number of invisible points are assigned initial feature values of zero, which weakens the ability of the image to effectively constrain the diffusion process. The subsequent variant, BDM [49], employs a pre-trained model to generate an output, which is then randomly combined with the PC² output to obtain the final reconstructed point cloud. However, the pre-trained model only provides a class-level reconstruction, and the random combination approach still lacks a targeted constraint.

3.2. 3D priors for Point Cloud Diffusion Models

To effectively constrain diffusion training and enhance reconstruction consistency, we propose a method that directly introduces object-level 3D priors to guide the training process. To comprehensively capture the 3D priors, we apply H camera rotation matrices in order to observe the initial point cloud from different viewpoints. The point cloud training data are obtained by running COLMAP [40, 41] on an image sequence captured around the object, with the input single-view image being part of this sequence. Using the rotation matrix of the input 2D image as a reference, we perform evenly spaced sampling of the image sequence to extract rotation matrices, ensuring that the point

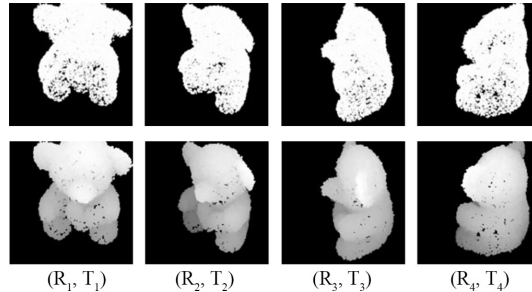


Figure 3. Illustration of rendered “teddybear” image from 4 different viewpoints. Top: rendered point cloud images. Bottom: rendered point cloud depth images.

clouds across the (H) viewpoints display significant variation. Based on the selected rotation matrices ($R_i, T_i, i \in H$), the initial point cloud x_0 is rotated and rendered to obtain point cloud images from multiple perspectives, as shown in the upper part of Fig. 3.

In this task, we consider that depth information is meaningful for 3D reconstruction (a hypothesis validated by our experimental results). Therefore, we designed a depth conversion algorithm that combines point cloud coordinates to further render point cloud depth maps, as illustrated in the lower part of Fig. 3. The depth images rendered from x_0 across different viewpoints serve as 3D priors to constrain the diffusion model’s training.

To effectively utilize the extracted 3D priors, we have attempted different strategies. Following PC² approach, where the features of multiple images are directly projected to the point cloud as conditions, causes an inconsistency in the number of conditions between the training and sampling phases, leading to model learning drift. A detailed analysis of this issue is provided in the supplementary materials 11.

To avoid the model learning drift problem, we strategically incorporate 3D priors as soft constraints during the training process. We formulate a bound term, named the 3D Prior Constraint, which continuously closes the data distribution between x_t and x_0 at each timestep t , thereby maximizing the ELBO. For implementation, the $R_i, T_i, i \in H$ matrices defined by the 3D priors are employed to rotate

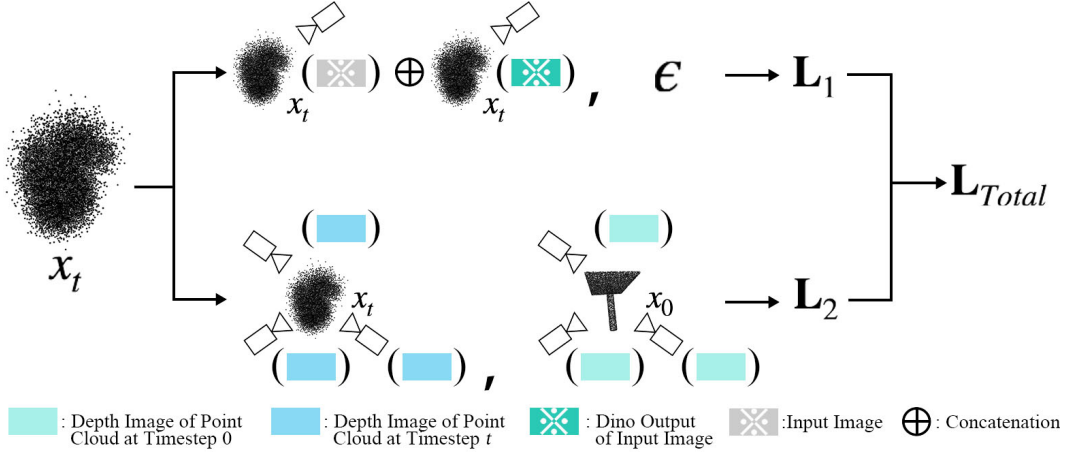


Figure 4. Illustrative structure for incorporating 2D and 3D priors. The 2D priors (upper part) are concatenated with the image features and mapped onto the point cloud as conditions. The 3D priors (lower part) are transformed into depth images of the point cloud at time steps x_0 and x_t . The bound term is transformed into the distances between corresponding depth images for increasing the ELBO.

the point cloud x_t , rendering it into H point cloud depth images. Mean Square Error (MSE) is then computed between the depth images of x_0 and x_t from the corresponding views. In our method, we retain the forward process but introduce a 3D Priors Constraint ($\|x_t - x_0\|^2$) to refine the reverse diffusion process:

$$\tilde{p}_\theta(x_{0:T}) := p(x_T) \prod_{t=1}^T p_\theta(x_{t-1}|x_t) e^{-\lambda \|x_t - x_0\|^2}. \quad (4)$$

Training is performed by optimizing the variational bound on negative log-likelihood.

$$\begin{aligned} L &= \mathbb{E}_q[-\log \tilde{p}_\theta(x_0)] \leq \mathbb{E}_q \left[-\log \frac{\tilde{p}_\theta(x_{0:T})}{q(x_{1:T}|x_0)} \right] \\ &= \mathbb{E}_q \left[\underbrace{\sum_{t=1}^T \mathcal{D}_{KL}(q(x_{t-1}|x_t, x_0) \| p_\theta(x_{t-1}|x_t))}_{L_{t-1}} \right. \\ &\quad \left. + \lambda \underbrace{\sum_{t=1}^T \|x_t - x_0\|^2}_{L_{3D \text{ Priors Constraint}}} + \underbrace{\mathcal{D}_{KL}(q(x_T|x_{t_0}) \| p(x_T))}_{L_T} \right. \\ &\quad \left. - \underbrace{\log p_\theta(x_0|x_T)}_{L_0} \right]. \quad (5) \end{aligned}$$

It can be derived from the formula that adding this term increases the ELBO, thereby facilitating the convergence of the diffusion model. The detailed derivation process of the function is provided in the supplementary materials 7. In this context, the enhanced convergence of the model effectively improves the consistency of the reconstruction, reducing the uncertainty associated with the generation process. The results in Fig. 5 intuitively support this conclusion. Due to the inherently disordered and sparse nature of 3D point cloud [14], the bound term $\|x_t - x_0\|^2$ is intractable. Consequently, the 3D priors are converted to 2D

depth images at timestep t to measure the distance between x_0 and x_t . v_i represents the camera parameter for viewpoint i . The objective after simplification is:

$$\begin{aligned} L(\theta) &:= \mathbb{E}_{\epsilon \sim \mathcal{N}(0, \mathbf{I})} \left[\underbrace{\|\epsilon - p_\theta(x_t, t, I, V)\|_2^2}_{\text{Diffusion Loss}} \right. \\ &\quad \left. + \sum_{i=1}^H \underbrace{\|\text{proj}(x_t, v_i) - \text{proj}(x_0, v_i)\|_2^2}_{\text{Priors Constraint}} \right]. \quad (6) \end{aligned}$$

The bound term computed between the point cloud depth maps at time step 0 and t from all H viewpoints are summed up. Then it is incorporated into the backpropagation process as a regularization term to constrain the model training and reinforce the reconstruction consistency. By simplifying the bound term to a basic MSE calculation, the additional computational overhead becomes negligible, ensuring that the training time of the model is not increased.

3.3. 2D priors for Point Cloud Diffusion Models

For single-image 3D point cloud reconstruction tasks, the image serves as the sole condition to guide the diffusion training, meaning that the information contained in the image directly influences the model's final performance. In various 2D vision tasks, the integration of strong priors has significantly improved model performance. Therefore, we also considered how to leverage existing models to further process the image, incorporating additional 2D priors to guide and constrain the training of the 3D point cloud diffusion model.

In terms of 2D global priors, we attempt to use OpenCLIP [5] to process the 2D images, extracting both text and image embeddings. These embeddings are then iteratively integrated into the model using a cross-attention structure similar to that in ControlNet [51]. However, the experimen-

tal results indicate that this approach does not yield any improvements. For 2D local priors, we utilize Zero123 [27] to generate multi-view images from the single 2D image. Unfortunately, due to the arbitrary camera angles of the 2D images, accurately estimating the camera (R, T) matrix of the generated images proved challenging. Consequently, the multi-view images can not be accurately aligned with the point cloud in this task. Further analysis and results are provided in the supplementary materials 6, 9 and 10.

Based on multiple attempts and experiments, we analyze that the 2D priors can only be extracted from the initial 2D image (I) and that the additional 2D priors can be integrated into the model training by overlaying them with the initial image features. Currently, the image information is primarily extracted using a pre-trained Vision Transformer (ViT) network [11], which captures features that mainly reflect planar texture characteristics. From our findings during the process of incorporating 3D priors, we consider that depth and contour information can provide more reliable guidance for 3D reconstruction. Therefore, we delve into the depth and contour information contained in the initial 2D image. We extract contours or estimate depth using DINO v2 [37]. Then, we overlay this information as additional 2D priors with the features outputted from the ViT, using concatenation for the integration of the 2D priors.

$$2D \text{ Priors} = F_I \oplus F_{I^*}, \quad (7)$$

where F_{I^*} represents the outputs of DINO v2. The top part of Fig. 4 illustrates the process of 2D priors incorporation, which facilitates the subsequent pixel-to-point mapping operation to assist in noise prediction. This approach effectively introduces additional 2D priors as a condition to guide the diffusion training.

4. Experiments

Dataset. To evaluate the effectiveness of our proposed method, we conduct experiments on two distinct datasets: the synthetic dataset ShapeNet [2, 8] and the real-world dataset Co3D [38]. ShapeNet dataset is a comprehensive collection of 3D computer-aided design models, covering 3,315 categories derived from the WordNet [36] database. In contrast, the Co3D dataset presents a challenging benchmark, as it consists of multi-view images of real-world objects from common object categories. We compare our results with PC² and BDM. Due to the high computational cost of using a class-level pre-trained model, BDM conducts experiments on only five categories in the ShapeNet dataset. Additionally, BDM neither performs experiments on the Co3D dataset nor provides checkpoints for the relevant pre-trained models. Our experimental setup is consistent with that of prior works in terms of image rendering, camera matrices, and train-test splits.

Metrics. The effectiveness of the reconstruction process is evaluated using two widely accepted metrics: Chamfer Distance (CD) and F-Score@0.01 (F1). CD quantifies the discrepancy between two point sets by calculating the shortest distance from each predicted point to its nearest point in the ground truth. To mitigate CD’s sensitivity to outliers, we also report the F-Score at a threshold of 0.01. In this metric, a reconstructed point is deemed accurately predicted if its nearest distance to any point in the ground truth point cloud falls within the specified threshold, providing a measure of precision in the reconstruction process.

	PC ²		CDM	
	CD ↓	F1 ↑	CD ↓	F1 ↑
airplane	65.97	0.655	59.72	0.660
bench	46.16	0.658	48.14	0.671
cabinet	54.87	0.454	53.54	0.464
car	64.36	0.547	63.92	0.558
chair	65.57	0.464	62.93	0.476
display	79.64	0.537	77.48	0.549
lamp	132.44	0.437	125.41	0.448
loudspeaker	83.79	0.392	84.74	0.393
rifle	29.37	0.776	27.20	0.791
sofa	47.54	0.472	45.33	0.492
table	73.87	0.527	67.95	0.547
telephone	48.33	0.671	49.61	0.674
watercraft	48.26	0.574	46.83	0.586
<i>Average</i>	64.63	0.551	62.52	0.562

Table 1. Performance comparison on ShapeNet.

Implementation Details. The aim is to maintain consistency across all settings in accordance with previous works. All images and rendering resolutions are set to 224×224 pixels. For the ShapeNet dataset, a total of 4,096 points are sampled for each 3D object, while for the Co3D dataset, 16,384 points are employed. Our method is implemented based on PC² using PyTorch. The PyTorch3D library is used to render the 3D prior images and handle rasterization during the projection conditioning phase. In the BDM experiments, all settings are kept at their original values, and PVD [52] is still utilized as the pre-trained model, with checkpoints sourced from the BDM code repository. During the 3D prior point cloud projection, we used a point size of 0.04 and projection images of 224×224 pixels. All experiments are conducted on a single GeForce RTX-4090.

4.1. Quantitative Results

ShapeNet. Since the ShapeNet dataset is synthetic, there is a distribution drift between its features and real-world data, leading to inaccurate depth estimation. Therefore, during the training process on this dataset, we use contour information as 2D priors and adopt planar features (the upper part of Fig. 3) in the 3D Priors Constraint. In Tab. 1, we present the results for the 13 classes in the widely used ShapeNet dataset, compared with PC². The results show a consistent

	airplane		car		chair		sofa		table		Average	
	CD ↓	F1 ↑										
PC ²	65.97	0.655	64.36	0.547	65.57	0.464	47.54	0.472	73.87	0.527	63.46	0.533
PC ² +BDM	59.04	0.660	65.85	0.559	64.21	0.485	44.12	0.504	68.35	0.551	60.31	0.552
CDM	59.72	0.660	63.92	0.558	62.93	0.476	45.33	0.492	67.95	0.547	59.97	0.547
CDM+BDM	57.35	0.665	60.44	0.569	58.54	0.497	42.81	0.512	64.17	0.568	56.66	0.562

Table 2. Performance comparison on ShapeNet. +BDM means using BDM during sampling.

improvement over those obtained with PC² on the ShapeNet dataset. This is particularly evident in the F1 score, indicating that our method demonstrates superior reconstruction capabilities across most categories.

As for Tab. 2, we compare our CDM with PC² and BDM. The BDM framework enables a reconstruction model and a pre-trained model to be sampled together during inference, incorporating random selection at some intermediate steps for fusing the two resulting point clouds. Due to the high computational cost of using a class-level pre-trained model, BDM only conducts experiments on five categories. In this experiment, our model also attempted to incorporate the priors from BDM’s pre-trained model. The results indicate that our model achieves the best performance without using the pre-trained model priors, and incorporating the pre-trained model can further improve the reconstruction results.

	PC ²		CDM	
	CD ↓	F1 ↑	CD ↓	F1 ↑
hydrant	92.32	0.485	90.11	0.507
teddybear	116.95	0.428	102.79	0.461
toytruck	153.84	0.421	125.40	0.474
Average	121.04	0.445	106.10	0.481

Table 3. Performance comparison on Co3D.

Co3D. In real-world scenarios, the 3D reconstruction performance of our method is illustrated in Tab. 3. The reconstructed objects display more detailed shapes and complex geometric configurations. We conducted experiments on the challenging Co3D dataset. Since BDM does not provide the relevant pre-trained models and has not been tested on this dataset, we only compared our method with PC² in this section, focusing on three categories. This outcome demonstrates the effectiveness of our method in addressing the challenges posed by real-world objects. Our proposed method shows superior performance across all object categories in both Chamfer Distance and F1 Score, indicating better geometric accuracy and precision in the 3D reconstructed models using just a single image.

Visualization. In this experiment, we present visual comparison results on the ShapeNet dataset. We compare our method with PC² and BDM across three categories of reconstruction. The first column of Fig. 5 displays the input images. We compare the reconstruction results from two

different viewpoints, with reconstruction errors of PC² and BDM are highlighted in red circles. Intuitively, the results from PC² exhibit ambiguities due to a lack of priors. For instance, in the first row, the sofa has two backs (Viewpoint 2), and in the third row, the table appears to have two layers (Viewpoint 1). In the case of BDM, the reconstruction results are significantly influenced by the non-specific object information introduced by class-level priors. For example, in the second row, a round tabletop is reconstructed (Viewpoint 1), while in the third row, the table legs are spaced too far apart (Viewpoint 2). In contrast, the object-level constraints of our method lead to higher details consistency between the reconstruction results and the input images. Additional visual comparisons, shown in Fig. 6 in the supplementary materials 8, further illustrate our model’s superior performance in maintaining reconstruction consistency.

4.2. Ablation Study

Leverage 2D and 3D Priors. We first verify the effectiveness of 2D and 3D priors. In Tab. 4, utilizing either 2D or 3D priors results in improved performance across the three categories in the Co3D dataset. This demonstrates the complementary strengths of 2D and 3D information in enhancing object reconstruction quality. Moreover, the combined priors configuration (2D + 3D) consistently outperforms other prior configurations across all categories, as shown by its superior performance in both Chamfer Distance (CD) and F1 metrics.

	teddybear		toytruck		hydrant		Average	
	CD ↓	F1 ↑	CD ↓	F1 ↑	CD ↓	F1 ↑	CD ↓	F1 ↑
Baseline	116.95	0.428	153.84	0.421	92.32	0.485	121.04	0.445
+2D	107.09	0.448	148.76	0.466	90.67	0.527	115.51	0.480
+3D	106.35	0.446	135.38	0.463	90.33	0.534	110.69	0.481
+2D+3D	102.79	0.461	125.40	0.474	90.11	0.507	106.10	0.481

Table 4. Ablation study of leveraging 2D and 3D priors.

3D Prior Frames and Point Size. Tab. 5 investigates the impact of the number of rendered point cloud images and the rendered point size in the 3D Priors Constraint on model performance. For simplicity, the results of these ablation experiments are evaluated using the Co3D “Teddybear” category. If the point size is insufficient, it can result in sparse point cloud rendering, which may lead to inaccurate distance calculations during projection rendering be-

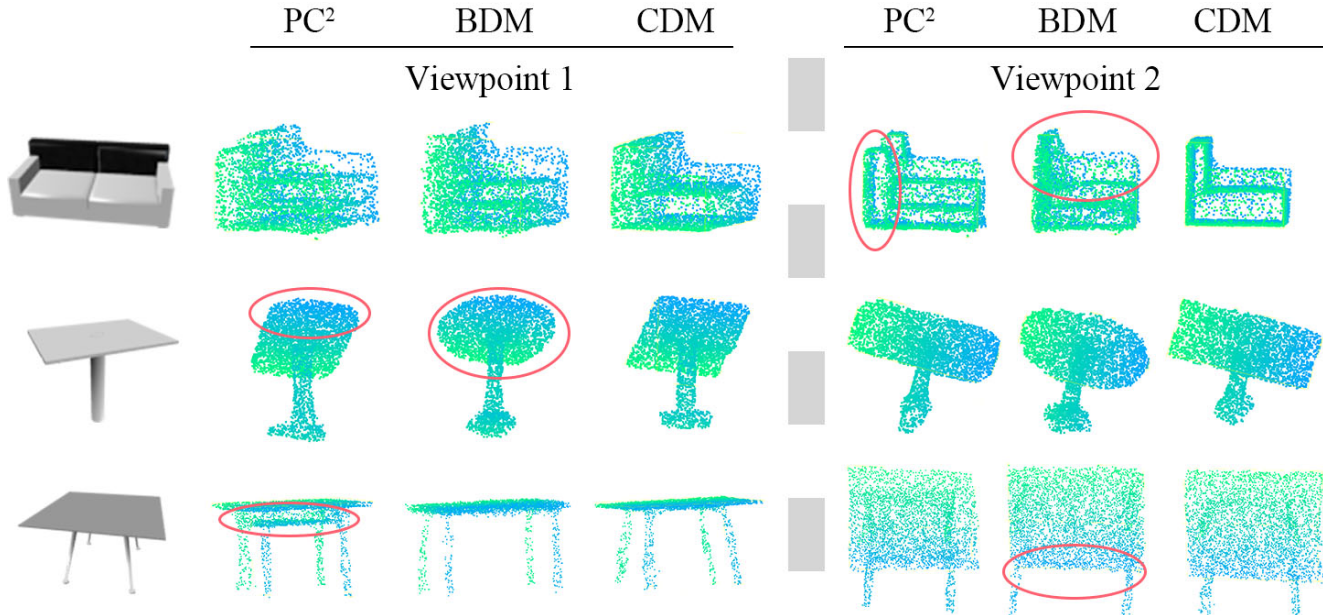


Figure 5. Visual comparison on the ShapeNet dataset. The first column displays the input image. We compare the reconstructed point clouds from two different viewpoints. Intuitively, PC^2 produces ambiguous results due to weak constraints, and BDM, which introduces class-level priors, fails to effectively control reconstruction consistency.

tween point clouds x_0 and x_t . The big number of frames is also a crucial factor in improving model performance. Increasing the number of rendered point cloud images allows for a more comprehensive description of the point cloud structure from a wider range of viewpoints.

Settings	F1 \uparrow
4 Frames + 0.04 point size	0.452
10 Frames + 0.0075 point size	0.451
10 Frames + 0.04 point size	0.461

Table 5. The impact of the number of camera rotations matrix (H) and rendered point size.

	Contour		Depth	
	CD \downarrow	F1 \uparrow	CD \downarrow	F1 \uparrow
ShapeNet				
airplane	59.72	0.660	62.37	0.655
chair	62.93	0.476	63.39	0.474
Co3D				
teddybear	106.48	0.451	102.79	0.461
<i>Average</i>	76.38	0.529	76.18	0.530

Table 6. Comparison of point cloud rendering methods. Airplane and chair are the ShapeNet category and Teddybear is in the Co3D category.

Rendering Methods of Point Cloud. In Tab. 6, we compare the effects of different 2D priors (depth and contour) on different kinds of datasets (real-world or synthetic).

The experimental results indicate that using contour as a 2D prior yields better performance on the ShapeNet (synthetic dataset), while depth proves to be a more effective 2D prior on the Co3D (real-world dataset). We attribute this difference to the features distribution of the two datasets. ShapeNet is an artificially synthesized dataset, which may introduce biases in depth information extraction, making the accurate contour information more beneficial for performance. In contrast, Co3D comprises images from real-world scenes, where accurate depth information is more advantageous for reconstruction.

5. Conclusion

This work proposes a Consistency Diffusion Model designed to enhance the model’s focus on reconstruction consistency. By extracting the inherent structural information from point cloud data, we introduce object-level 3D priors to constrain the model learning. Specifically, we propose a new bound term that leverages these 3D priors to increase the ELBO, reducing the uncertainty of the diffusion model, and reinforcing consistency. Additionally, we extract depth and contour information from the input image as additional 2D priors, effectively guiding and constraining the training process. We conducted extensive comparative experiments to evaluate the effectiveness of different priors and incorporation strategies. The experimental results consistently show that our method achieves SOTA performance in both synthetic and real-world scenarios. For future work, we

plan to integrate the reconstructed point cloud with textual descriptions for point cloud editing.

References

- [1] Joseph J Atick, Paul A Griffin, and A Norman Redlich. Statistical approach to shape from shading: Reconstruction of three-dimensional face surfaces from single two-dimensional images. *Neural computation*, 8(6):1321–1340, 1996. 2
- [2] Angel X Chang, Thomas Funkhouser, Leonidas Guibas, Pat Hanrahan, Qixing Huang, Zimo Li, Silvio Savarese, Manolis Savva, Shuran Song, Hao Su, et al. Shapenet: An information-rich 3d model repository. *arXiv preprint arXiv:1512.03012*, 2015. 6
- [3] Anpei Chen, Zexiang Xu, Fuqiang Zhao, Xiaoshuai Zhang, Fanbo Xiang, Jingyi Yu, and Hao Su. Mvsnerf: Fast generalizable radiance field reconstruction from multi-view stereo. In *ICCV*, pages 14124–14133, 2021. 2
- [4] Jun-Kun Chen, Jipeng Lyu, and Yu-Xiong Wang. Neuraleditor: Editing neural radiance fields via manipulating point clouds. In *CVPR*, pages 12439–12448, 2023. 1
- [5] Mehdi Cherti, Romain Beaumont, Ross Wightman, Mitchell Wortsman, Gabriel Ilharco, Cade Gordon, Christoph Schuhmann, Ludwig Schmidt, and Jenia Jitsev. Reproducible scaling laws for contrastive language-image learning. In *CVPR*, pages 2818–2829, 2023. 5, 1
- [6] German KM Cheung, Simon Baker, and Takeo Kanade. Visual hull alignment and refinement across time: A 3d reconstruction algorithm combining shape-from-silhouette with stereo. In *CVPR*, pages II–375. IEEE, 2003. 2
- [7] Christopher B Choy, Danfei Xu, JunYoung Gwak, Kevin Chen, and Silvio Savarese. 3d-r2n2: A unified approach for single and multi-view 3d object reconstruction. In *ECCV*, pages 628–644. Springer, 2016. 2
- [8] Christopher B Choy, Danfei Xu, JunYoung Gwak, Kevin Chen, and Silvio Savarese. 3d-r2n2: A unified approach for single and multi-view 3d object reconstruction. In *ECCV*, 2016. 6
- [9] Sammy Christen, Wei Yang, Claudia Pérez-D’Arpino, Otmar Hilliges, Dieter Fox, and Yu-Wei Chao. Learning human-to-robot handovers from point clouds. In *CVPR*, pages 9654–9664, 2023. 1
- [10] Yan Di, Chenyangguang Zhang, Pengyuan Wang, Guangyao Zhai, Ruida Zhang, Fabian Manhardt, Benjamin Busam, Xi-angyang Ji, and Federico Tombari. Ccd-3dr: Consistent conditioning in diffusion for single-image 3d reconstruction. *arXiv preprint arXiv:2308.07837*, 2023. 3
- [11] Alexey Dosovitskiy. An image is worth 16x16 words: Transformers for image recognition at scale. *arXiv preprint arXiv:2010.11929*, 2020. 6
- [12] George Fahim, Khalid Amin, and Sameh Zarif. Single-view 3d reconstruction: A survey of deep learning methods. *Computers & Graphics*, 94:164–190, 2021. 2
- [13] Kui Fu, Jiansheng Peng, Qiwen He, and Hanxiao Zhang. Single image 3d object reconstruction based on deep learning: A review. *MTA*, 80(1):463–498, 2021. 2
- [14] Yulan Guo, Hanyun Wang, Qingyong Hu, Hao Liu, Li Liu, and Mohammed Bennamoun. Deep learning for 3d point clouds: A survey. *ITPAMI*, 43(12):4338–4364, 2020. 5
- [15] Richard Hartley and Andrew Zisserman. *Multiple view geometry in computer vision*. Cambridge university press, 2003. 2
- [16] Philipp Henzler, Jeremy Reizenstein, Patrick Labatut, Roman Shapovalov, Tobias Ritschel, Andrea Vedaldi, and David Novotny. Unsupervised learning of 3d object categories from videos in the wild. In *CVPR*, pages 4700–4709, 2021. 1, 2
- [17] Berthold KP Horn. Shape from shading: A method for obtaining the shape of a smooth opaque object from one view. 1970. 2
- [18] Wonbong Jang and Lourdes Agapito. Codenerf: Disentangled neural radiance fields for object categories. In *ICCV*, pages 12949–12958, 2021. 1, 2
- [19] Mohammad Mahdi Johari, Yann Lepoittevin, and François Fleuret. Geonerf: Generalizing nerf with geometry priors. In *CVPR*, pages 18365–18375, 2022. 2
- [20] Abhishek Kar, Christian Häne, and Jitendra Malik. Learning a multi-view stereo machine. *NIPS*, 30, 2017. 2
- [21] Hiroharu Kato and Tatsuya Harada. Learning view priors for single-view 3d reconstruction. In *CVPR*, pages 9778–9787, 2019. 2
- [22] Jonáš Kulháněk, Erik Derner, Torsten Sattler, and Robert Babuška. Viewformer: Nerf-free neural rendering from few images using transformers. In *ECCV*, pages 198–216. Springer, 2022. 2
- [23] Xueting Li, Sifei Liu, Kihwan Kim, Shalini De Mello, Varun Jampani, Ming-Hsuan Yang, and Jan Kautz. Self-supervised single-view 3d reconstruction via semantic consistency. In *ECCV*, pages 677–693. Springer, 2020. 2
- [24] Chen-Hsuan Lin, Oliver Wang, Bryan C Russell, Eli Shechtman, Vladimir G Kim, Matthew Fisher, and Simon Lucey. Photometric mesh optimization for video-aligned 3d object reconstruction. In *CVPR*, pages 969–978, 2019. 1
- [25] Minghua Liu, Ruoxi Shi, Linghao Chen, Zhuoyang Zhang, Chao Xu, Xinyue Wei, Hansheng Chen, Chong Zeng, Jiayuan Gu, and Hao Su. One-2-3-45++: Fast single image to 3d objects with consistent multi-view generation and 3d diffusion. *arXiv preprint arXiv:2311.07885*, 2023. 3
- [26] Minghua Liu, Chao Xu, Haian Jin, Linghao Chen, Mukund Varma T, Zexiang Xu, and Hao Su. One-2-3-45: Any single image to 3d mesh in 45 seconds without per-shape optimization. *NIPS*, 36, 2024. 3
- [27] Ruoshi Liu, Rundi Wu, Basile Van Hoorick, Pavel Tokmakov, Sergey Zakharov, and Carl Vondrick. Zero-1-to-3: Zero-shot one image to 3d object, 2023. 3, 6
- [28] Yunze Liu, Yun Liu, Che Jiang, Kangbo Lyu, Weikang Wan, Hao Shen, Boqiang Liang, Zhoujie Fu, He Wang, and Li Yi. Hoi4d: A 4d egocentric dataset for category-level human-object interaction. In *CVPR*, pages 21013–21022, 2022. 1
- [29] Yuan Liu, Sida Peng, Lingjie Liu, Qianqian Wang, Peng Wang, Christian Theobalt, Xiaowei Zhou, and Wenping Wang. Neural rays for occlusion-aware image-based rendering. In *CVPR*, pages 7824–7833, 2022. 2

- [30] Yuan Liu, Cheng Lin, Zijiao Zeng, Xiaoxiao Long, Lingjie Liu, Taku Komura, and Wenping Wang. Syncdreamer: Generating multiview-consistent images from a single-view image. *arXiv preprint arXiv:2309.03453*, 2023. 3
- [31] Shitong Luo and Wei Hu. Diffusion probabilistic models for 3d point cloud generation. In *CVPR*, pages 2837–2845, 2021. 3
- [32] Zhaoyang Lyu, Zhifeng Kong, Xudong Xu, Liang Pan, and Dahua Lin. A conditional point diffusion-refinement paradigm for 3d point cloud completion. *arXiv preprint arXiv:2112.03530*, 2021. 3
- [33] Luke Melas-Kyriazi, Christian Rupprecht, and Andrea Vedaldi. Pc2: Projection-conditioned point cloud diffusion for single-image 3d reconstruction. In *CVPR*, pages 12923–12932, 2023. 2, 3, 4
- [34] Lars Mescheder, Michael Oechsle, Michael Niemeyer, Sebastian Nowozin, and Andreas Geiger. Occupancy networks: Learning 3d reconstruction in function space. In *CVPR*, pages 4460–4470, 2019. 1
- [35] Ben Mildenhall, Pratul P Srinivasan, Matthew Tancik, Jonathan T Barron, Ravi Ramamoorthi, and Ren Ng. Nerf: Representing scenes as neural radiance fields for view synthesis. *CACM*, 65(1):99–106, 2021. 2
- [36] George A. Miller. WordNet: A lexical database for English. In *Human Language Technology: Proceedings of a Workshop held at Plainsboro, New Jersey, March 8-11, 1994*, 1994. 6
- [37] Maxime Oquab, Timothée Darcet, Théo Moutakanni, Huy Vo, Marc Szafraniec, Vasil Khalidov, Pierre Fernandez, Daniel Haziza, Francisco Massa, Alaaeldin El-Nouby, et al. Dinov2: Learning robust visual features without supervision. *arXiv preprint arXiv:2304.07193*, 2023. 2, 6
- [38] Jeremy Reizenstein, Roman Shapovalov, Philipp Henzler, Luca Sbordone, Patrick Labatut, and David Novotny. Common objects in 3d: Large-scale learning and evaluation of real-life 3d category reconstruction. In *ICCV*, 2021. 6
- [39] Konstantinos Rematas, Ricardo Martin-Brualla, and Vittorio Ferrari. Sharf: Shape-conditioned radiance fields from a single view. *arXiv preprint arXiv:2102.08860*, 2021. 1, 2
- [40] Johannes L Schonberger and Jan-Michael Frahm. Structure-from-motion revisited. In *CVPR*, pages 4104–4113, 2016. 4
- [41] Johannes L Schönberger, Enliang Zheng, Jan-Michael Frahm, and Marc Pollefeys. Pixelwise view selection for unstructured multi-view stereo. In *ECCV*, pages 501–518. Springer, 2016. 4
- [42] Ruoxi Shi, Hansheng Chen, Zhuoyang Zhang, Minghua Liu, Chao Xu, Xinyue Wei, Linghao Chen, Chong Zeng, and Hao Su. Zero123++: a single image to consistent multi-view diffusion base model. *arXiv preprint arXiv:2310.15110*, 2023. 1
- [43] Omid Taheri, Nima Ghorbani, Michael J Black, and Dimitrios Tzionas. Grab: A dataset of whole-body human grasping of objects. In *ECCV*, pages 581–600. Springer, 2020. 1
- [44] Maxim Tatarchenko, Stephan R Richter, René Ranftl, Zhuwen Li, Vladlen Koltun, and Thomas Brox. What do single-view 3d reconstruction networks learn? In *CVPR*, pages 3405–3414, 2019. 2
- [45] Arash Vahdat, Francis Williams, Zan Gojcic, Or Litany, Sanja Fidler, Karsten Kreis, et al. Lion: Latent point diffusion models for 3d shape generation. *NIPS*, 35:10021–10039, 2022. 3
- [46] Bram Wallace and Bharath Hariharan. Few-shot generalization for single-image 3d reconstruction via priors. In *ICCV*, pages 3818–3827, 2019. 1
- [47] Andrew P Witkin. Recovering surface shape and orientation from texture. *Artificial intelligence*, 17(1-3):17–45, 1981. 2
- [48] Haozhe Xie, Hongxun Yao, Shengping Zhang, Shangchen Zhou, and Wenxiu Sun. Pix2vox++: Multi-scale context-aware 3d object reconstruction from single and multiple images. *IJCV*, 128(12):2919–2935, 2020. 2
- [49] Haiyang Xu, Yu Lei, Zeyuan Chen, Xiang Zhang, Yue Zhao, Yilin Wang, and Zhuowen Tu. Bayesian diffusion models for 3d shape reconstruction. In *CVPR*, pages 10628–10638, 2024. 2, 3, 4
- [50] Alex Yu, Vickie Ye, Matthew Tancik, and Angjoo Kanazawa. pixelnerf: Neural radiance fields from one or few images. In *CVPR*, pages 4578–4587, 2021. 1, 2
- [51] Lvmin Zhang, Anyi Rao, and Maneesh Agrawala. Adding conditional control to text-to-image diffusion models. In *ICCV*, pages 3836–3847, 2023. 5, 1, 3
- [52] Linqi Zhou, Yilun Du, and Jiajun Wu. 3d shape generation and completion through point-voxel diffusion. In *ICCV*, pages 5826–5835, 2021. 6
- [53] Linqi Zhou, Yilun Du, and Jiajun Wu. 3d shape generation and completion through point-voxel diffusion. In *ICCV*, pages 5826–5835, 2021. 3

Consistency Diffusion Models for Single-Image 3D Reconstruction with Priors

Supplementary Material

6. More Ablation Study Results

Image and Text Embedding for Global Features. Table 7 presents an ablation study evaluating different global feature conditioning methods. We investigate two combination strategies: concatenation (\oplus) and cross-attention (\otimes). The results show that both concatenation and cross-attention reduce model performance, indicating that global features may not effectively enhance the model in this context. Therefore, in our method, the image encoder is dedicated solely to extracting local features from the image, while the diffusion backbone handles both local and global feature extraction from the point cloud.

Diffusion Model Conditions	F1 \uparrow
1 Image feature	0.428
2 Image feature \oplus OpenCLIP (text)	0.230
3 Image feature \oplus OpenCLIP (image)	0.320
4 Image feature \oplus OpenCLIP (depth image)	0.421
5 Image feature \otimes OpenCLIP (image)	0.423
6 Image feature \otimes OpenCLIP (text)	0.379

Table 7. Comparison of different types of features and utilization strategies. \oplus means concatenation and \otimes means cross attention.

More kinds of Conditions in Training. As demonstrated in Tab. 8, utilizing varying numbers or different kinds of rendered images as conditions yields different outcomes. The results in rows 2, 3, and 4 demonstrate that directly projecting the additional image priors (generated using ControlNet [51]) onto the point cloud significantly degrades performance. Even when using only ground truth (GT) images for projection, as shown in row 5, there is no improvement in performance. This issue arises from the mismatch in conditioning between the training and sampling phases, leading to a drift in the model’s learning process. Hence, directly projecting priors to complement the point cloud’s initial features may not be an effective strategy. If the input single image is replaced with one generated by ControlNet, as shown in rows 6 and 7, inaccuracies in the generated image features also lead to a decline in performance. A detailed description of the experiments using images generated by ControlNet can be found in Section 11.

7. Function Derivation

The derivation of Eq. 5, which introduces the reduced-variance variational bound for diffusion models within the context of our reverse process, is presented following Eq. 8.

Conditions	F1 \uparrow
1 1 GT image	0.428
2 1 GT image and 3 ControlNet images	0.423
3 1 GT image and 1-3 ControlNet	0.416
4 4 Gray ControlNet images	0.425
5 4 GT images	0.420
6 1 ControlNet image	0.413
7 1 ControlNet Gray image	0.425

Table 8. Comparison of priors utilization strategies.

8. Visual Comparison on Co3D Dataset

Fig. 6 presents additional visual results. We compare our method with PC² on the Co3D dataset. The first column on the left displays the input images. By comparing from two different viewpoints, it is intuitively evident that PC²’s reconstruction results exhibit significant ambiguity and missing parts in areas that are not visible from the viewpoint. In contrast, our method maintains strong consistency with the input images.

9. Global priors Knowledge Embedding

In this work, we try to extract global priors from a single 2D image. By feeding the image into OpenCLIP [5], we obtain both text and image embeddings. We then employ a multi-scale cross-attention mechanism, inspired by the ControlNet architecture, to iteratively integrate these OpenCLIP priors into the network. Tab. 7 presents the results of embedding these global priors. From the experimental results, we observe that embedding either type of prior (text or image embedding) individually or jointly does not enhance performance and may even lead to a decline. We analyze this outcome and conclude that, for the 3D point cloud reconstruction task, global information provides only a rough understanding of the object, while detailed features are essential for effective reconstruction. Consequently, we shift our focus to exploring how to incorporate more detailed priors into the reconstruction process.

10. Local priors Knowledge Embedding

On the local feature level, we experiment with using Zero123++ [42] to generate images of the target object from various angles based on a single 2D image. The aim is to project features from these multi-view images onto the point cloud after rotating the cloud, thereby increasing the number of points with initial features. However, during our

$$\begin{aligned}
L &= \mathbb{E}_q [-\log \tilde{p}_\theta(x_0)] \leq \mathbb{E}_q \left[-\log \frac{\tilde{p}_\theta(x_{0:T})}{q(x_{1:T}|x_0)} \right] \\
&= \mathbb{E}_q \left[-\sum_{t=1}^T \log \tilde{p}_\theta(x_{t-1}|x_t, x_0) - \log p_\theta(x_T) + \sum_{t=1}^T \log q(x_t|x_{t+1}) \right] \\
&= \mathbb{E}_q \left[-\sum_{t=1}^T \log p_\theta(x_{t-1}|x_t, x_0) - \lambda \sum_{t=1}^T \|x_t - x_0\|^2 - \log p_\theta(x_T) + \sum_{t=1}^T \log q(x_t|x_{t+1}) \right] \\
&= \mathbb{E}_q \left[\sum_{t=1}^T \underbrace{\mathcal{D}_{KL}(q(x_{t-1}|x_t, x_0) \| p_\theta(x_{t-1}|x_t))}_{L_{t-1}} - \lambda \sum_{t=1}^T \underbrace{\|x_t - x_0\|^2}_{L_{3D \text{ Priors Constraint}}} + \underbrace{\mathcal{D}_{KL}(q(x_T|x_0) \| p(x_T))}_{L_T} - \underbrace{\log p_\theta(x_0|x_T)}_{L_0} \right]
\end{aligned} \tag{8}$$

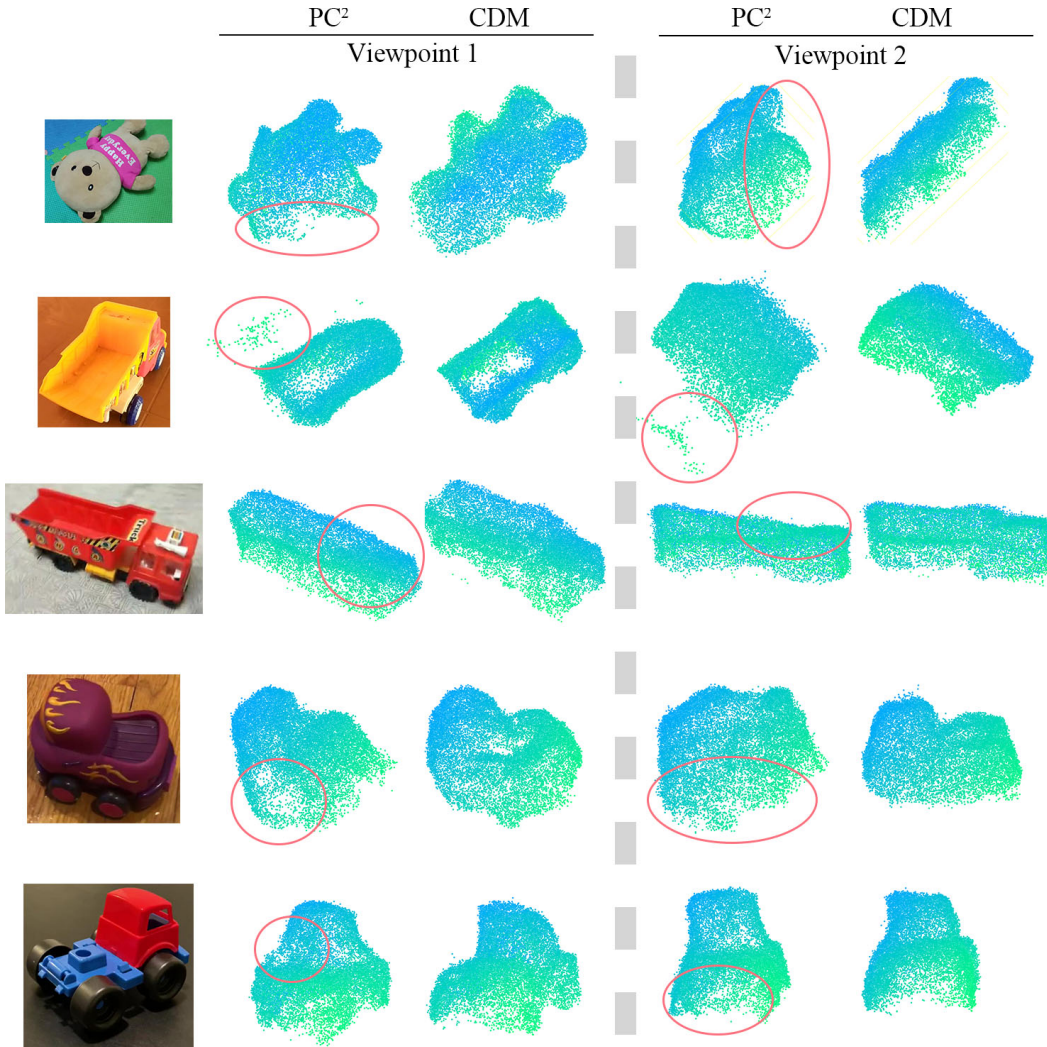


Figure 6. Visual comparison on the Co3D dataset. The first column displays the input image. We compare the reconstructed point clouds from two different viewpoints. Intuitively, PC² produces ambiguous results due to weak constraints.

experiments, we found that due to the arbitrary nature of the 2D image’s camera parameters and the uncalibrated po-

sition of the image relative to the target object, the camera parameters of the images generated by Zero123++ are

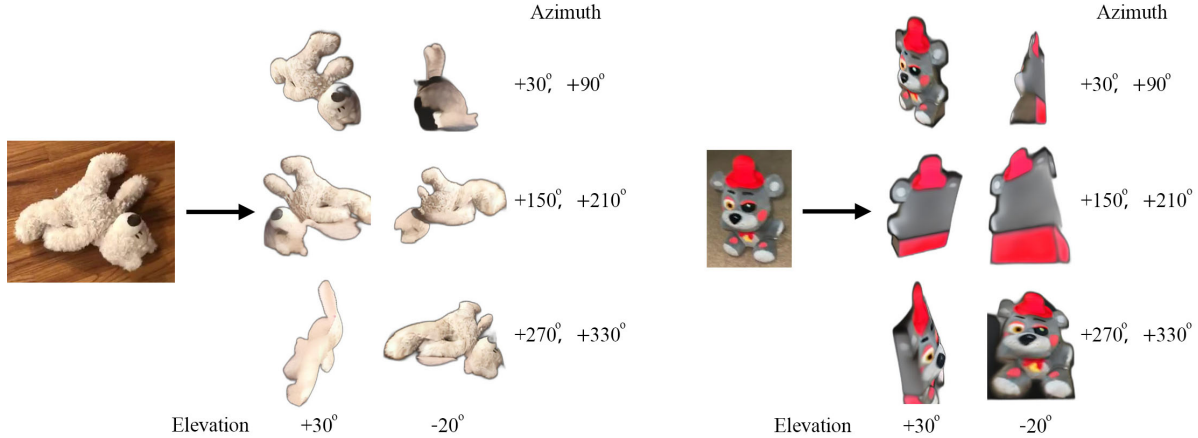


Figure 7. Illustration of the generation results of the zero123++ on the “teddybear” category in the Co3D dataset. zero123++ generates images of the target object from six fixed viewpoints. However, due to the arbitrary positioning of the target object, the generated images frequently contain ambiguities, and the object’s structure appears errors.

often difficult to estimate accurately. This makes it challenging to rotate the point cloud to match the input image correctly, preventing effective pixel-to-point feature mapping. As shown in Fig. 7, when a single image is input, the zero123++ method can only generate reconstructed images from a fixed viewpoint, which exhibit significant deformation. Consequently, these generated images not only cannot be aligned with the point cloud using the camera rotation matrices, but they also introduce a considerable amount of erroneous information.

11. Directly Introduce 2D Priors

Based on our experiments with both global and local priors, we conclude that the key to effectively incorporating 2D priors is to stack these priors directly onto the single input image. Therefore, we straightforwardly follow the training approach of PC², mapping the depth map features from different angles to the point cloud through pixel-to-point projection. To ensure consistency with the original 2D image used as a condition, we fine-tuned ControlNet [51] using multi-view point cloud images. This fine-tuning enables ControlNet to generate corresponding 2D texture images from the point cloud images, as illustrated in Fig. 8. Subsequently, we used the generated 2D images to assign features to the initial point cloud x_0 . As a result, on average, 97% of the points in x_0 now have initial features, significantly addressing the issue of many points having zero initial features due to occlusions from a single viewpoint. This enhancement provides a stronger constraint for reconstruction. Tab. 8 presents a comparison of the reconstruction results using this approach.

Our comparative analysis reveals that while adding more conditions increases the proportion of point cloud points

with initial features, it ultimately results in a decline in model performance during the sampling stage. This unexpected outcome drew our attention and prompted further investigation. We believe this issue arises from the mismatch in the number of conditions between the training and sampling phases, resulting in a deviation in the model’s learning process. To the best of our knowledge, no prior work has proposed or discussed the impact of inconsistent numbers of conditions during training and sampling. We refer to this resulting issue as “model learning drift.” This phenomenon occurs because, during training, the model relies on multiple conditions to guide its learning effectively. However, during sampling, we lack access to the initial point cloud and cannot generate additional images through ControlNet as conditions by rotating the point cloud. Consequently, only one image is available as a condition during sampling.

Therefore, we abandoned the idea of directly introducing priors and instead focused on how to incorporate prior knowledge softly into the network training. Based on this motivation, we propose a method in this work that converts the inherent 3D structure priors of the training data into a supervisory loss. This loss continually helps the network improve reconstruction consistency, leading to better reconstruction results.

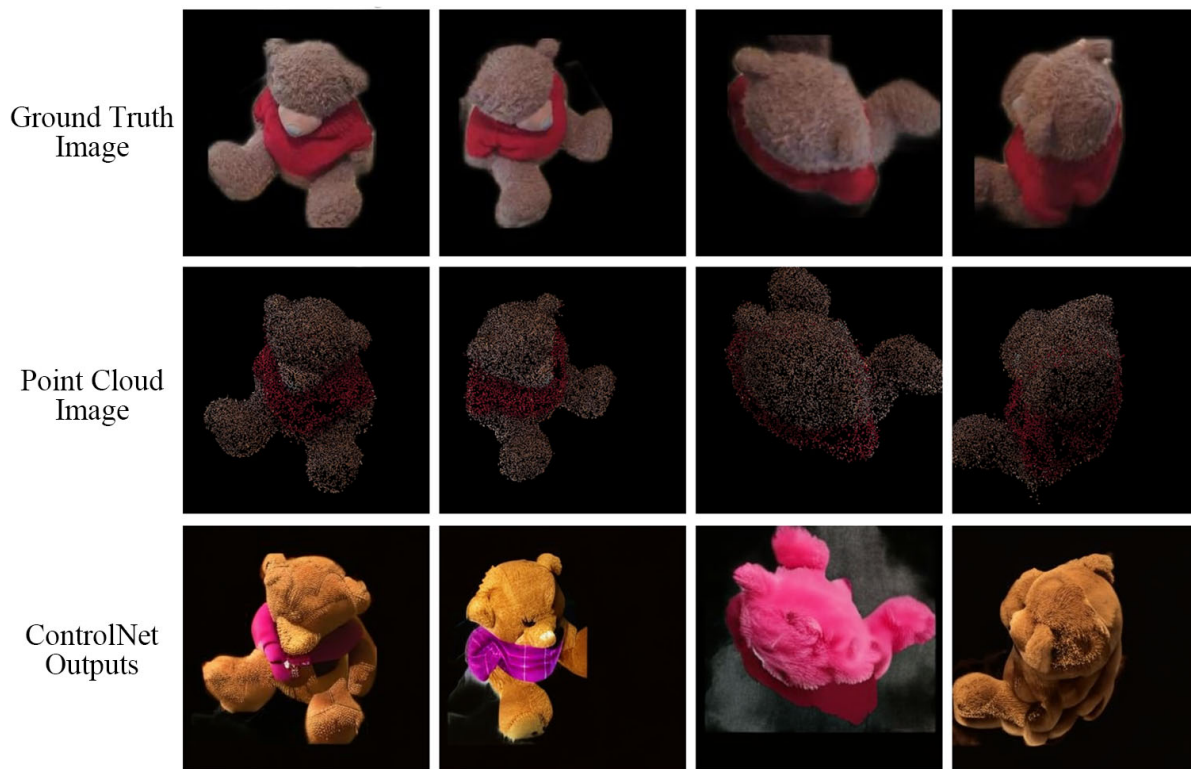


Figure 8. Illustration of ControlNet outputs after fine-tuning. The first row shows the ground truth (GT) input images, and the second row displays the rendered point cloud images from the same viewpoint. We pair the images from the first and second rows corresponding to the same viewpoint for fine-tuning ControlNet. The third row contains the outputs after fine-tuning ControlNet. This fine-tuning approach ensures that the shapes of the output images are completely consistent with the GT images.